

# The hidden architecture of equilibrium self-assembly

Maximilian C. Hübl<sup>1</sup>, Thomas E. Videbæk<sup>2</sup>, Daichi Hayakawa<sup>2</sup>,  
W. Benjamin Rogers<sup>2\*</sup>, Carl P. Goodrich<sup>1\*</sup>

<sup>1</sup>Institute of Science and Technology Austria (ISTA), Am Campus 1, Klosterneuburg,  
3400, Austria.

<sup>2</sup>Martin A. Fisher School of Physics, Brandeis University, Waltham, 02453,  
Massachusetts, USA.

\*Corresponding author(s). E-mail(s): [wrogers@brandeis.edu](mailto:wrogers@brandeis.edu); [carl.goodrich@ist.ac.at](mailto:carl.goodrich@ist.ac.at);  
Contributing authors: [maximilian.huebl@ist.ac.at](mailto:maximilian.huebl@ist.ac.at); [videbaek@brandeis.edu](mailto:videbaek@brandeis.edu);  
[dhayakawa@brandeis.edu](mailto:dhayakawa@brandeis.edu);

## Abstract

Experiments have reached a monumental capacity for designing and synthesizing microscopic particles for self-assembly, making it possible to precisely control particle concentrations, shapes, and interactions. However, we lack a comprehensive inverse-design framework for tuning these particle-level attributes to obtain desired system-level assembly outcomes, like the yield of a user-specified target structure. This severely limits our ability to take full advantage of this vast design space to assemble nanomaterials with complex structure and function. Here we show that a hidden mathematical architecture controls equilibrium assembly outcomes and provides a single comprehensive view of the entire design space. This architecture predicts which structures can be assembled at high yield and reveals constraints that govern the coexistence of structures, which we verify through detailed, quantitative assembly experiments of nanoscale particles synthesized using DNA origami. Strong experimental agreement confirms the importance of this underlying architecture and motivates its use as a predictive tool for the rational design of self-assembly. These results uncover a universal core logic underpinning all equilibrium self-assembly that forms the basis for a robust inverse-design framework, applicable to a wide array of systems from biological protein complexes to synthetic nanomachines.

**Keywords:** self-assembly, DNA origami, inverse-design, convex polyhedra

To control self-assembly is to suppress the formation of unwanted structures. For more than a decade, attaining such control through increasingly specific binding rules (Fig. 1a) has been the foundational pillar of both theoretical and experimental studies of programmable self-assembly. The resulting experimental platforms with specifically designed binding rules are vast, including DNA-based particles (*e.g.* DNA-coated colloids [1–5], DNA-tiles [6–9], or DNA-origami [10–

16]), particles with shape-specificity [17, 18], *de novo* designed proteins [19, 20], and magnetic-handshake particles [21], among others. The more restrictive the binding rules, the more off-target structures can be avoided: In the so-called fully-addressable limit, each particle type appears only once in the final structure, and only the target structure (and subsets of it) are allowed.

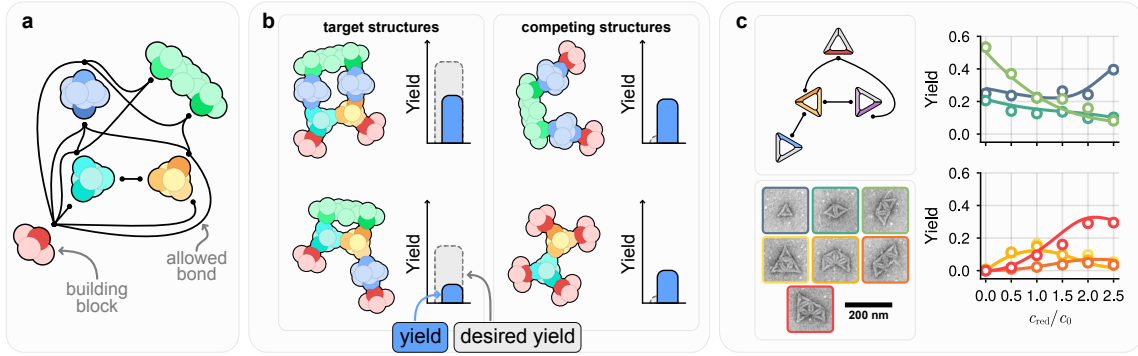


**Fig. 1** Semi-addressable self-assembly leads to competition between distinct structures. (a) A semi-addressable assembly system with highly promiscuous binding. The particles’ programmable binding sites are sketched in darker colors, and binding rules are indicated with black lines. Only sites that are connected by black lines are allowed to bind. (b) Sketch of some of the structures that can form from the particles in (a). How close to a given desired yield distribution can we come by optimizing chemical potentials, binding energies, and temperature? (c) Measured (points) and theoretical (lines) yields of all observed structure shapes resulting from the triangular particles and binding rules shown on the top-left. Colors of the points and lines correspond to the color outline around the seven observed structure shapes. Yields are shown as a function of the concentration  $c_{red}$  of the red particle species. Each other particle species is supplied at concentration  $c_0$ . Error bars show the standard error of the measured yield, and are generally smaller than the plot markers. See Methods and SI for details.

More recently, experiments have challenged this conventional wisdom, showing that comparable self-assembly yields can be obtained using smaller numbers of particle species [13, 22–24], even when doing so introduces the possibility of off-target competing structures [25]. Not only is this “semi-addressable” regime more economical, as it requires fewer particle species to be synthesized, but it enables the possibility to assemble multiple multifarious or “shape-shifting” structures from a single pool of building blocks [9, 22, 26–28]. However, the semi-addressable regime demands additional control to offset the presence of off-target competing structures (Fig. 1b), often requiring delicate tuning of particle concentrations and binding energies. The challenge is that these control variables have subtle and often counterintuitive effects on the assembly outcome, making it difficult to predict not only *how* to assemble a particular structure at high yield, but *if* high-yield assembly is even possible at all.

Here, we show that a series of hidden thermodynamic constraints not only answers these questions, but constitutes a fundamental mathematical structure, which we call an architecture, describing equilibrium self-assembly that can be readily exploited for inverse design. This architecture comes from the intimate correspondence between the constraints and high-dimensional

convex polyhedra, and is hidden because the constraints only appear in a certain asymptotic limit even though their effects are far-reaching. Exploiting this architecture leads to a theoretical framework for equilibrium self-assembly, through which we can exhaustively enumerate all (sets of) structures that can be assembled at high yield by adjusting the chemical potentials and binding energies of the particles, determine the possible relative yields between all structures, and design and predict the outcome of multifarious assemblies far from the fully-addressable limit. To test our framework, we design and synthesize a set of DNA-origami particles, and perform experiments to self-assemble a set of multifarious ring-shaped structures. Without *a priori* knowledge of the binding energies or particle concentrations, our theory is able to quantitatively predict the possible relative yields of the coexisting multifarious structures under various conditions. Taken together, our results demonstrate a hidden internal logic to equilibrium self-assembly, and provide a powerful framework for inverse design in a wide range of experimental settings.

## Uncovering hidden thermodynamic constraints in the ‘asymptotic limit’

We consider the equilibrium self-assembly of particles that interact through short-ranged binding sites. As shown in Fig. 1a, a system is composed of  $d_{\text{spc}}$  particle species, and the interactions follow specific binding rules with  $d_{\text{bnd}}$  allowed bond types. The binding rules determine the set of possible structures  $\mathcal{S}$  that can form. We assume for now that the total number of possible structures,  $n_{\text{str}} = |\mathcal{S}|$ , is finite, and that we are in possession of a complete enumeration of all structures, as obtained, for example, through the methods in Refs. [25, 29]. The yield of each structure at temperature  $T$  depends on the  $d_{\text{spc}}$  chemical potentials for each species,  $\boldsymbol{\mu}$ , and the  $d_{\text{bnd}}$  binding energies of each bond type,  $\boldsymbol{\varepsilon}$ . To keep notation compact, we combine these parameters into a single,  $d$ -dimensional parameter vector  $\boldsymbol{\xi} = (k_{\text{B}}T)^{-1}[\boldsymbol{\mu}, \boldsymbol{\varepsilon}]^T$ , where  $d = d_{\text{spc}} + d_{\text{bnd}}$  and  $k_{\text{B}}$  is Boltzmann’s constant.

In equilibrium, the yield of any structure can be computed from the partition function. The number density of structure  $s$  is given by

$$\rho_s(\boldsymbol{\xi}) = \Omega_s e^{\boldsymbol{M}_s \cdot \boldsymbol{\xi}}, \quad (1)$$

where  $\Omega_s$  is a positive pre-factor related to the symmetry and entropy of  $s$ , and  $\boldsymbol{M}_s \in \mathbb{N}^d$  is a vector listing how many particle species and bonds of each type are present in  $s$  (see Methods) [30, 31]. The equilibrium yield is then just

$$Y_s(\boldsymbol{\xi}) = \frac{\rho_s(\boldsymbol{\xi})}{\sum_{s' \in \mathcal{S}} \rho_{s'}(\boldsymbol{\xi})}, \quad (2)$$

where the sum in the denominator is the partition function. Figure 1c and the related discussion in Methods demonstrates that these expressions lead to highly accurate and robust predictions of experimental yields.

A common goal is to assemble a structure at high yield, while suppressing everything else. Therefore, we begin by asking: *for which structures  $s$  can tuning the chemical potentials and binding energies  $\boldsymbol{\xi}$  lead to yields  $Y_s$  approaching unity?* This question immediately leads to a simple but far-reaching observation. Due to the exponential dependence of  $\rho_s$  on  $\boldsymbol{\xi}$  (Eq. (1)), a structure density can only vanish if  $\|\boldsymbol{\xi}\| \rightarrow \infty$ . Therefore, to

achieve high target yield by suppressing off-target structures, we need to consider *limits* in the grand canonical parameter space. To make this clear, we rewrite the parameters as  $\lambda \hat{\boldsymbol{\xi}}$ , where  $\|\hat{\boldsymbol{\xi}}\| = 1$  and  $\lambda$  is a scalar that we can make arbitrarily large. Note that this is a seemingly diabolical limit because as the binding energies diverge, so too do the equilibration times. Nevertheless, we will see that this limit implies thermodynamic constraints that have profound implications even as we pull back to experimentally relevant energy scales.

In the limit of large  $\lambda$ , the structure densities are

$$\lim_{\lambda \rightarrow \infty} \rho_s(\lambda \hat{\boldsymbol{\xi}}) = \begin{cases} \infty & \text{if } \boldsymbol{M}_s \cdot \hat{\boldsymbol{\xi}} > 0 \\ \Omega_s & \text{if } \boldsymbol{M}_s \cdot \hat{\boldsymbol{\xi}} = 0 \\ 0 & \text{if } \boldsymbol{M}_s \cdot \hat{\boldsymbol{\xi}} < 0. \end{cases} \quad (3)$$

Importantly, the first case,  $\boldsymbol{M}_s \cdot \hat{\boldsymbol{\xi}} > 0$ , is unphysical as it implies a diverging number of structures per unit volume, meaning that steric effects make it impossible to reach the limit  $\lambda \rightarrow \infty$  (Methods). Excluding these unphysical directions leads to  $n_{\text{str}}$  thermodynamic constraints on  $\hat{\boldsymbol{\xi}}$ , one for each possible structure  $s$ , in the asymptotic limit:

$$\boldsymbol{M}_s \cdot \hat{\boldsymbol{\xi}} \leq 0. \quad (4)$$

These constraints and Eq. (3) point us toward the exact answer to our initial question: a structure  $s$  can only be assembled at 100% yield if there exists a  $\hat{\boldsymbol{\xi}}$ , such that  $\boldsymbol{M}_s \cdot \hat{\boldsymbol{\xi}} = 0$  and  $\boldsymbol{M}_{s'} \cdot \hat{\boldsymbol{\xi}} < 0$  for all other structures  $s'$ . We call such a structure *asymptotically designable*, or simply *designable*. If  $\boldsymbol{M}_s \cdot \hat{\boldsymbol{\xi}} = 0$  for multiple structures, then all corresponding yields remain finite in the asymptotic limit, and together we call them a *designable set*.

Physically,  $\boldsymbol{M}_s \cdot \hat{\boldsymbol{\xi}} = 0$  means that the entropic cost of adding the necessary particles to  $s$ , which is set by the chemical potentials, is balanced by the bond energy of  $s$ . This causes the number density of  $s$  to be unaffected by uniform rescaling of the parameters, which makes it possible for  $s$  to survive in the limit  $\lambda \rightarrow \infty$ .

## Constraint cones and the architecture of designable sets

We now show that asymptotically designable sets are related to each other through an underlying

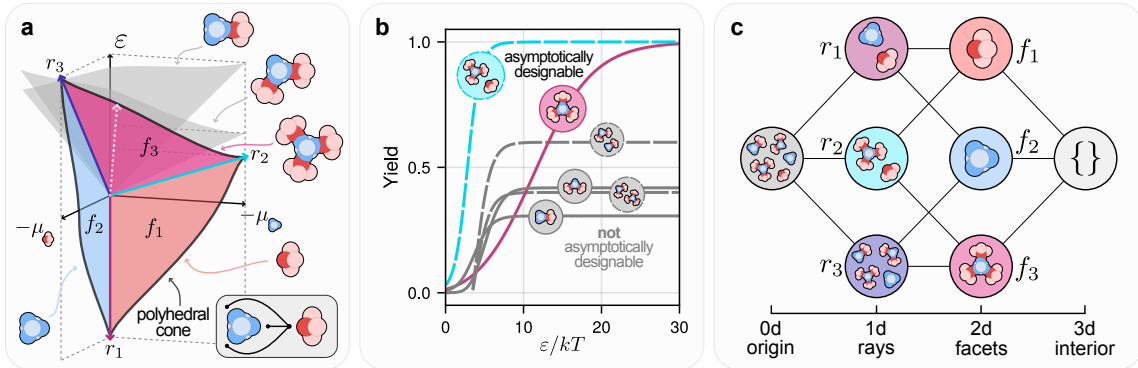


**Fig. 2** Constraint planes reveal a hidden architecture. (a) The constraint planes and polyhedral cone derived from the simple binding rules shown in the bottom right. The parameter space consists of the binding energy  $\varepsilon$  (defined here to be the same for all bonds) and the chemical potentials  $\mu$  of the two particle species. Non-redundant constraints are shown in color, redundant constraints are shown in gray. The white dotted line shows a limit direction parallel to the face  $f_3$ . (b) Yield of various structures (solid) and pairs of structures (dashed) as a function of binding energy  $\varepsilon$ . For the two asymptotically designable (sets of) structures, yields were computed by following limiting directions within their corresponding faces on the constraint cone (the white dotted line and the ray  $r_2$  in (a)). Non-designable yields were optimized numerically. See SI for additional information. (c) The faces of the polyhedral cone in (a), visualized as a Hasse diagram. Every vertex corresponds to a polyhedral face, which in turn corresponds to a designable set of structures. The edges indicate containment relations.

mathematical structure, or architecture, determined by the constraints (Eq. (4)). Consider the pedagogical example shown in Fig. 2a, where  $d = 3$  parameters control the assembly of 5 structures. Each structure has a corresponding constraint that restricts the allowed limit directions  $\hat{\xi}$  to a given half-space defined by Eq. (4). Geometrically, the allowed region of parameter space forms a *convex polyhedral cone*, or constraint cone, whose boundary is composed of constraint planes. In Fig. 2a, this boundary is determined by three 2-dimensional “faces” given by the blue, pink, and red planes.

If we set  $\hat{\xi}$  to align with one of these three planes, then  $M_s \cdot \hat{\xi} = 0$  for the corresponding structure and  $M_s \cdot \hat{\xi} < 0$  for all others, making the structure asymptotically designable. For example, set  $\hat{\xi}$  to align with the white dotted line in Fig. 2a, which is on the  $f_3$  face corresponding to the tetramer. The purple curve in Fig. 2b shows the yield of the tetramer as a function of the binding energy  $\varepsilon$ , which is proportional to  $\lambda$  as we go along the limiting direction. As expected for designable structures, the yield approaches 1 as  $\lambda \rightarrow \infty$ . Similarly, both monomers are also designable.

The boundary of the constraint cone also includes the intersections of the planes. These

1-dimensional faces, or rays, identify sets of structures that are together designable. For example, if  $\hat{\xi}$  aligns with the extremal ray  $r_2$ , then  $M_s \cdot \hat{\xi} = 0$  for both the red monomer and the tetramer, meaning they form a designable set. We can see this by the cyan curve in Fig. 2b, where we set  $\hat{\xi}$  to align with ray  $r_2$  and find that the combined yield of the red monomer and tetramer approaches 1 as  $\lambda \rightarrow \infty$ .

Importantly, the two constraint planes shown in gray do not appear on their own anywhere on the boundary of the constraint cone—they are *redundant* constraints. This means that the dimer and trimer are not designable and can never be assembled at 100% yield, even in the asymptotic limit. The gray curves in Fig. 2b shows the maximum achievable yield of the dimer, trimer, and a few non-designable pairs of structures, as a function of  $\varepsilon$  (see SI for details). In all cases, the maximum yield is well below 1. However, the constraint planes for the dimer and trimer do intersect with the constraint cone precisely at ray  $r_3$ , meaning they are part of a larger asymptotically designable set, one that contains all structures except the red monomer.

These ideas are made mathematically precise in Methods. For now, however, the essential point is that the boundary of the constraint cone is

composed of many different faces,  $f$ , whose dimensionality can vary from  $d_f = 0$  to  $d_f = d$ , and each face corresponds to an asymptotically designable set of structures,  $\mathcal{S}_f$ .

The geometry of the constraint cone naturally leads to a combinatorial architecture of the designable sets. This architecture stems from the fact that the faces of the constraint cone are not independent: lower dimensional faces are always *contained* in higher dimensional ones. For example,  $r_1$  in Fig. 2a is contained in both  $f_1$  and  $f_2$ . This means that the structures in  $\mathcal{S}_{f_1}$  and  $\mathcal{S}_{f_2}$  must also appear in  $\mathcal{S}_{r_1}$ . These containment relations also imply that *the intersection of two designable sets is again a designable set* (see SI). This means that the designable sets are nested within each other and can be partially ordered by the containment relations of the constraint cone.

This combinatorial architecture of designable sets can be visualized with a so-called *Hasse diagram*, as shown in Fig. 2c. Every vertex in this diagram corresponds to a polyhedral face/designable set and the edges indicate the containment relations. The designable sets naturally order into levels determined by the dimension  $d_f$  of the corresponding face. The Hasse diagram is a direct visualization of *all* sets of structures that can be assembled at high yield by tuning chemical potentials and binding energies.

Using algorithms from polyhedral computation (Methods), we can identify all designable sets even in highly non-trivial cases. Consider the binding rules shown in Fig. 3a, which we will investigate in detail throughout the rest of this paper. Besides 280 open structures, these particles can form three closed rings: a hexagon, a rhomboid, and a triangle (Fig. 3b). Since this system contains a total of  $d = 9$  parameters (4 chemical potentials and 5 binding energies), we cannot directly visualize the constraint cone. Nevertheless, out of  $2^{283} - 1$  candidate sets, we can identify all 1672 designable sets and visualize their combinatorial architecture through a Hasse diagram (Fig. 3c).

Figure 3b highlights some of the containment relations. While the hexagonal and triangular rings are individually designable, as is the set of all three rings combined, the rhomboid ring by itself is not and can only be assembled as part of a larger set. Traversing the diagram further towards the left leads to larger and larger encompassing designable sets.

## Hidden constraints determine relative yields

The mathematical architecture revealed by the polyhedral cone and the Hasse diagram also enables us to identify lower-dimensional design spaces that govern relative yields of various structures. To see this, consider any set of parameters  $\xi$  together with a particular face of the polyhedral cone  $f$  and its corresponding designable set of structures  $\mathcal{S}_f$ . We can decompose  $\xi$  into two parts,

$$\xi = \lambda \hat{\xi}_f + \xi_{\perp}, \quad (5)$$

where  $\lambda \hat{\xi}_f$  is the  $d_f$  dimensional component of  $\xi$  that is parallel to the face  $f$  and  $\xi_{\perp}$  is the  $c_f \equiv d - d_f$  dimensional component that is perpendicular to  $f$ .

As long as  $\xi_{\perp}$  does not diverge with  $\lambda$ , it does not affect the designability of the structures, and all structures not in  $\mathcal{S}_f$  still vanish as  $\lambda \rightarrow \infty$ . The primary difference is that the number densities of structures in  $\mathcal{S}_f$  become

$$\rho_s = \Omega_s e^{\mathbf{M}_s \cdot \xi_{\perp}} \quad (6)$$

instead of just  $\rho_s = \Omega_s$  (see Eq. (3)). Thus, we can use  $\xi_{\perp}$  to tune the relative yields within  $\mathcal{S}_f$ .

Importantly, since  $\mathbf{M}_s \cdot \hat{\xi}_f = 0$ , Eq. (6) is accurate for any  $\lambda$ . Since  $\xi_{\perp}$  is normal to the face  $f$ , the number densities of the structures in  $\mathcal{S}_f$  can be tuned with precisely  $c_f = d - d_f$  degrees of freedom. Therefore, the ostensibly hidden thermodynamic constraints lead to a low-dimensional design space of relative yields in experimentally relevant settings. Furthermore, since  $\lambda$  controls the absolute yield of  $\mathcal{S}_f$  by suppressing all other structures, the relative yields within a designable set can be tuned *independently* of its absolute yield. This is a key property of designable sets that distinguishes them from non-designable sets.

These facts allow us to make highly nontrivial and falsifiable predictions. Consider the three closed rings in Fig. 3, which together form a designable set with  $d_f = 7$  and  $c_f = 2$ . Although the number densities of the three rings can be tuned with  $c_f = 2$  degrees of freedom, in this case, their relative yields can only be tuned with a single degree of freedom. This is because one of the two degrees of freedom simply raises the total particle concentration uniformly and therefore does not

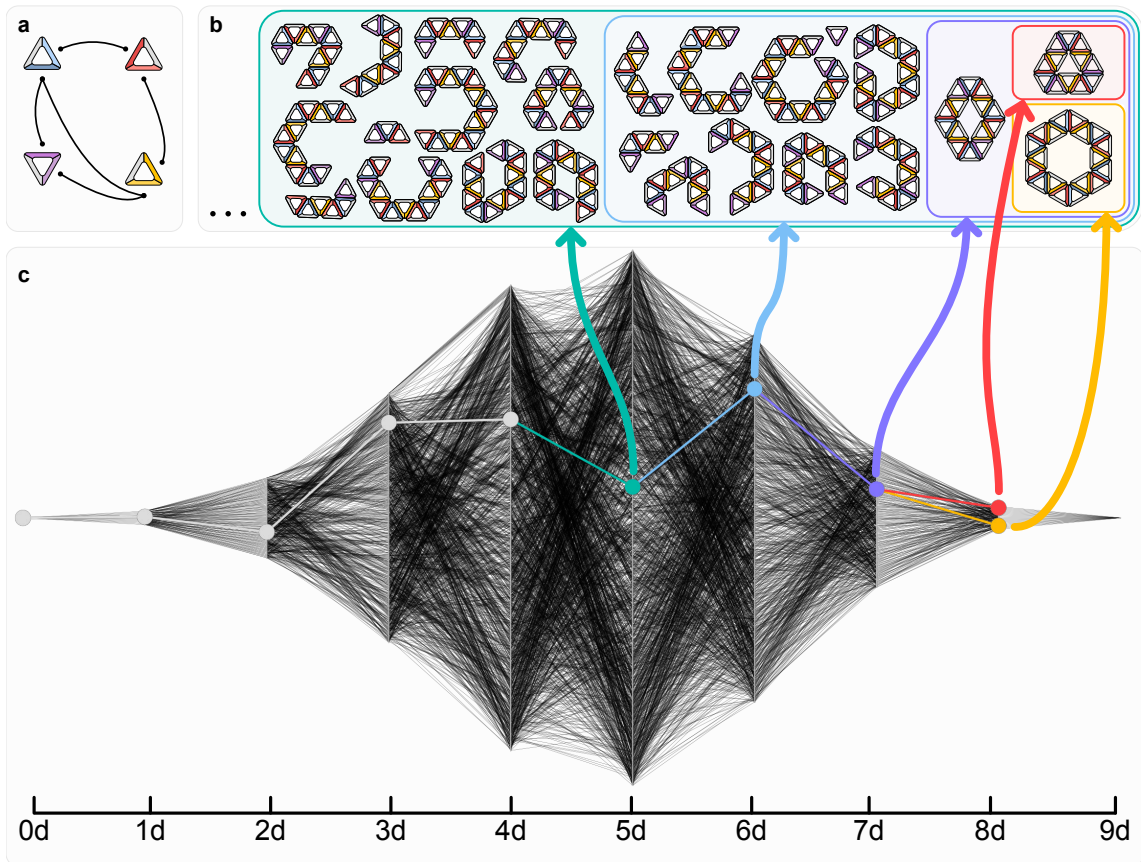


**Fig. 3** The architecture of a nine-dimensional design space. (a) Binding rules between four triangular particles.  $\xi$  consists of four chemical potentials and five binding energies. (b) Some of the structures that are allowed by the binding rules in (a). Structures are grouped into hierarchical designable sets, showing clear containment relations. (c) The Hasse diagram corresponding to the nine-dimensional constraint cone reveals an intricate and highly nontrivial architecture. An example path from the two designable closed structures (yellow and red) to the set of all structures  $\mathcal{S}$  is highlighted.

affect relative yields (Methods). Figure 4a shows the relative yields of these three structures as a function of the  $c_f - 1 = 1$ -dimensional component of  $\xi$ , which we label  $\zeta_{\perp}$ . No matter how the parameters are chosen, thermodynamically allowed relative yields should follow these curves, whose shapes are determined by structure compositions and entropy (Methods). We now test this prediction experimentally.

### Experiments corroborate the hidden architecture

We now introduce an experimental system to explore the real-world implications of our theory. We synthesize triangular particles using DNA

origami, and implement the specific binding rules shown in Fig. 3a by extending single-stranded DNA from the triangles' sides. Adjusting the sequences of these strands then allows us to program specific interactions by exploiting Watson-Crick base pairing, and folding monomers with various combinations of edge strands allows us to create different "colors" of particles, or species (see SI for sequence information). We then perform assembly experiments by mixing the various particle types with concentrations between 10 nM and 50 nM for an individual particle type in a buffer that has 20–30 mM of  $\text{MgCl}_2$ . By annealing these assembly mixtures from 40–25 °C with a ramp rate of 0.1 °C/1.5 h, we ensure that we

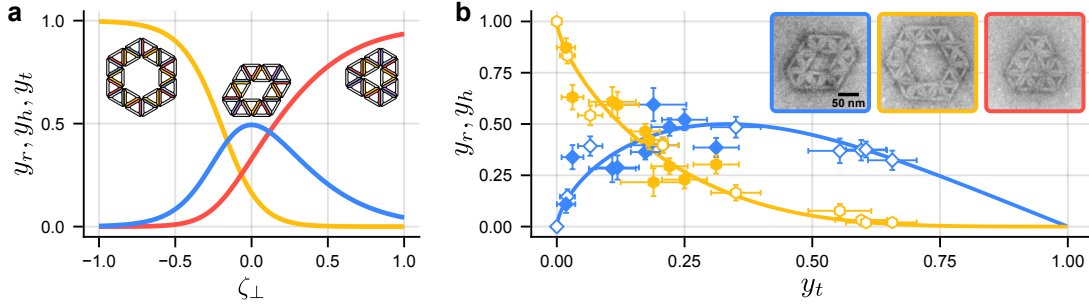


**Fig. 4** Quantitative experimental validation of the reduced design space. (a) Relative yield space of rhomboid ( $y_r$ , blue), hexagon ( $y_h$ , yellow), and triangular ( $y_t$ , orange) rings. Shown are the relative yields  $y_i = Y_i/(Y_{tri} + Y_{rho} + Y_{hex})$ , as a function of the one degree of freedom  $\zeta_{\perp}$  in parameter space that affects the relative yields. (b) Comparison between experimentally measured (points) and theoretically predicted (lines) relative yields of the three rings. Since we do not know the value of  $\zeta_{\perp}$  in experiments,  $y_r$  and  $y_h$  are shown as a function of  $y_t$ . Empty symbols correspond to equal interactions, full symbols correspond to enhanced binding between some bonds as defined in the text. Different data points are obtained at varying concentrations of the purple particle  $c_p$  (see Fig. 3a) and  $MgCl_2$  concentrations. Error bars show the standard error of the measured relative yields. See SI for details.

pass through the temperature at which the interactions are weak and reversible, and the structures can anneal. After annealing is complete, we image the assembly result using transmission electron microscopy (TEM), allowing us to count different structure shapes to measure their relative yields.

To test our prediction that there is only a single degree of freedom with which relative yields of the closed rings can be tuned, we perform multiple experiments at different parameter values, changing the concentration of purple particles  $c_p$  (see Fig. 3a) and the relative binding energy of the bonds between purple, blue, and yellow particles with respect to the bonds between the red, blue, and yellow particles. Since the value of  $\zeta_{\perp}$  (see Fig. 4a) is unknown in experiments, we re-plot the different yield curves of Fig. 3a against each other, showing the normalized yields of the hexagonal and rhomboidal rings as a function of the triangular ring. In this way, we can directly compare our theoretical results to experimental data.

Figure 4b shows excellent agreement between our theoretical expectations and experimental results. The lines show the theoretically predicted relative yields, whereas the experimentally measured relative yields are shown with different markers, according to the experimental parameter values. Every data point corresponds to between 50–150 countable structures. This striking quantitative agreement between theory and experiment,

which is achieved without any fit parameters and with minimal assumptions on the particle interactions (see Methods), confirms that the mathematical architecture leads to robust experimental predictions.

Moreover, this agreement is obtained very far from the asymptotic limit, with absolute yields of the rings ranging from about 0.1–0.4%. This confirms the key finding of the paper: equilibrium self-assembly is governed by an underlying architecture that restricts which yield combinations are allowed. For example, even with 9 parameters, the three yields in Fig. 4 cannot be tuned independently. Our ability to not only understand but precisely calculate this underlying architecture makes it a powerful tool for experimentally accurate inverse design.

## Conclusions

We have shown that two critically important questions in self-assembly—what structures can be assembled at high yield? and to what extent can relative yields be manipulated?—are both governed by an inherent mathematical architecture. In the asymptotic limit of large binding energies and chemical potentials, a limit necessary for achieving high yields, a series of thermodynamic constraints naturally emerges that together constrain these parameters to the interior of a high-dimensional polyhedral cone and allows us to

exhaustively enumerate all structures or structure sets that are designable. Each set corresponds to a face of the polyhedral cone, and the normal to this face determines the relative yields of these structures, allowing us to calculate the reduced design space of structures within a set. Importantly, this latter result does not require taking the asymptotic limit, and leads to quantitative yield predictions that we have verified experimentally using self-assembling DNA-origami particles.

The excellent experimental agreement that we find in Fig. 4 demonstrates the validity and utility of our analysis. The underlying mathematical architecture, which is determined directly from the binding rules, does indeed govern equilibrium self-assembly. The only assumptions here are 1) there exists a finite set of possible structures that can form, and 2) the prefactor  $\Omega_s$  in Eq. (1) does not strongly depend on the binding energies and chemical potentials. These assumptions are satisfied in a wide variety of experimental systems, including our DNA-origami particles, for which highly-specific DNA interactions at discrete binding sites create orientationally locking bonds, making it possible to enumerate all structures directly from the binding rules [25].

Furthermore, knowledge of this architecture, enabled by efficient methods of polyhedral computation, presents a powerful, accurate, and useful framework for inverse design. This framework is complimentary to other developments in the field, as overwhelming focus has been placed on engineering the discrete binding rules (*e.g.* Fig. 1a) to suppress the possibility of off-target structures. Our analysis works within the context of a given set of binding rules, showing if and how the assembly process can be further controlled.

To see how this framework might be exploited in practice, start with one or more target structures with the goal of assembling them at high yield. For a proposed set of binding rules, our calculations enable a comprehensive and near-instantaneous view of the entire design space. We simply read out whether or not the target structures are designable, allowing us to quickly reject binding rules for which the best-case yield is insufficiently small. For example, we can immediately reject the binding rules in Fig. 3a if we want to assemble the rhomboid on its own. However, these binding rules are excellent if our goal is to

dynamically switch between the hexagon and triangle, as this can be achieved by moving along the low-dimensional design space  $\zeta_{\perp}$ .

Interestingly, note that the existence of such low-dimensional design spaces of relative yields, like the one in Fig. 4a, is not inevitable. If the constraint planes were placed randomly, then all designable sets would contain only structures that are themselves designable. In this scenario, a structure would either be designable or not part of any designable set, and lower-dimensional design spaces would generically not exist. This outcome is not what we see; instead, the constraint plane of non-designable structures usually intersects the polyhedral cone at some lower-dimensional face (*e.g.*, the dimer and trimer in Fig. 2, or the rhomboid in Fig. 3). These structures are therefore part of a relatively small designable set, with a lower-dimensional design space that we can calculate.

Our results raise a number of important and interesting questions. First and foremost, does self-assembly far from equilibrium conform to similar constraints? While counterexamples surely exist, it will be interesting to learn whether the architecture provides a useful starting point for understanding and designing non-equilibrium systems. Furthermore, has evolution exploited this architecture to better achieve robust and economical assembly? A better understanding of the dynamical processes that govern the approach to equilibrium or the drive away from equilibrium will help to address these questions more thoroughly, opening new doors to the design and control of dissipative pathways to synthetic assembly, as well as new understanding of self-organization in living systems.

## Methods

### Yield calculations

The vector  $\mathbf{M}_s$  that appears in Eq. (1) counts the number of species and bond types present in structure  $s$ . If the structure contains  $n_s^{\alpha}$  particles of species  $\alpha$ , and  $b_s^a$  bonds of bond type  $a$ , then  $\mathbf{M}_s = [n_s^1, \dots, n_s^{d_{\text{spc}}}, b_s^1, \dots, b_s^{d_{\text{bond}}}]^T$ .

The pre-factor  $\Omega_s$  is the entropic partition function of a structure  $s$ , and is given by

$$\Omega_s = \frac{Z_s^{\text{vib}} Z_s^{\text{rot}}}{\lambda^{D n_s} \sigma_s}, \quad (7)$$

where  $Z_s^{\text{vib}}$  and  $Z_s^{\text{rot}}$  are the vibrational and rotational partition functions [30, 31] of  $s$  respectively,  $\lambda^D$  is the volume of a phase space cell,  $\sigma_s$  is the symmetry number of  $s$ , and  $n_s = \sum_{\alpha} n_s^{\alpha}$  is the number of particles in  $s$ . If the microscopic interactions between particles are known,  $\Omega_s$  can be computed using the methods in Refs. [30–32]. We assume  $\Omega_s$  to be independent of  $\xi$ , which is exactly true for simple interaction models, such as those in Ref. [25], and a good assumption in general, since the effect of the parameters on structure entropy is much weaker than their contribution in the Boltzmann weight, Eq. (1). For the DNA-origami particles that we study here, models of the DNA-mediated binding interactions suggest that the binding entropy and energy can, to some extent, be tuned independently [16].

When enumerating structures in this paper, we assume that bond stiffness is very high, such that building blocks can only fit together side-to-side and strained structures cannot form. This assumption could in principle be relaxed, in which case the partition function for a strained structure would carry an additional factor  $e^{-\varepsilon_{\text{strain}}/kT}$ , set by the strain energy  $\varepsilon_{\text{strain}}$ .

Figure 1c shows that equilibrium yields as predicted by Eq. (1) agree excellently with the experimental yields. We have realized the particles and binding rules shown on the left-hand side of Fig. 1c with DNA origami (the details of which are discussed below and in the SI), and we measured the yields of the seven possible structure shapes as a function of the concentration  $c_{\text{red}}$  of the particle species shown in red. All other particle species were kept at  $c_{\text{blue}} = c_{\text{yellow}} = c_{\text{purple}} = c_0$ , with  $c_0 = 2$  nM. The binding energies of all four bond types were designed to be the same in the experiments. Because the value of the binding energy is unknown, we use it as a fit parameter in our theoretical calculations. Minimizing the least-squares error between the yields predicted by Eq. (1) and the experimental yields, we obtain optimal agreement at a fit binding energy of approximately  $12.1 k_{\text{B}}T$ . This value is in

line with previous experimental estimates of the binding energy for DNA-origami triangles [12, 15].

## Thermodynamic constraints

To see why diverging structure densities in the asymptotic limit are unphysical, note that an infinite density of structures implies an infinite density of particles. For parameters violating  $\mathbf{M}_s \cdot \hat{\xi} \leq 0$ , particle concentrations *rise* as  $\lambda$  is increased, meaning that to realize the asymptotic limit, more and more particles need to be added to the system. At some point, steric effects, which are not explicitly modeled here, make it impossible to add more particles, which means that chemical potentials cannot be raised further, making it impossible to reach the asymptotic limit.

This situation is similar to, but distinct from, other cases where unphysical chemical potentials emerge, such as standard aggregation theory [33], or *e.g.* degenerate Bose gases [34]. In these cases, unphysical chemical potentials arise due to singularities in the partition function, while in our case (assuming a finite number of possible structures) the forbidden chemical potentials come from the imposition of the asymptotic limit in parameter space.

## Asymptotic designability and the constraint cone

### Designable sets and polyhedral faces

We now give more precise definitions to the concepts discussed in the main text. All of the following definitions are discussed at length in any reference on convex polyhedra, such as Refs. [35–38].

A polyhedral face  $f$  is a subset of a polyhedron where certain constraints are active ( $\mathbf{M}_s \cdot \hat{\xi} = 0$  for  $s \in \mathcal{S}_f$ ), and all other constraints are inactive ( $\mathbf{M}_s \cdot \hat{\xi} < 0$  for  $s \notin \mathcal{S}_f$ ). The faces of a polyhedral cone can have any dimension from  $d_f = 0$  to  $d_f = d$ . Comparing this definition with the definition of designable sets, Eq. (3), shows that the directions in parameter spaces that lead to high-yield assembly for a designable set  $\mathcal{S}_f$  correspond one-to-one with the polyhedral face  $f$  whose active equalities correspond to the structures in  $\mathcal{S}_f$ .

Faces of a polyhedron can be partially ordered by inclusion, and the resulting partially ordered

set is called the polyhedron’s *face lattice*. The combinatorial properties of the face lattice give rise to the combinatorial properties of designable sets, which are discussed in the main text.

The polyhedral architecture also has important computational implications. Since all constraints are linear, checking whether a (set of) structure(s) is asymptotically designable can be done exactly and efficiently with linear programming [39], while the enumeration of designable sets can be achieved with algorithms from polyhedral computation, as shown below.

### Interpretation of constraint cone geometry

To obtain an intuitive understanding of how the geometry of the constraint cone determines what can and cannot be assembled at high yield, consider again the example in Fig. 2a. Pick a limiting direction  $\hat{\xi}$  that is inside or on the surface of the constraint cone, so that the thermodynamic constraints are satisfied. Taking the high- $\lambda$  limit, any structure whose corresponding constraint is active ( $\mathbf{M}_s \cdot \hat{\xi} = 0$ ) will be assembled at finite density, while all other structures, whose constraints are inactive ( $\mathbf{M}_s \cdot \hat{\xi} < 0$ ), will vanish. Those structures that can be assembled at 100% yield individually therefore correspond to regions of the cone where their corresponding constraint is the only active one. These regions are just the bounding (hyper-)planes of the cone, denoted by  $f_1, f_2, f_3$  in Fig. 2a. To every bounding hyperplane therefore corresponds an asymptotically designable structure<sup>1</sup>.

Importantly, not every structure’s constraint corresponds to a bounding hyperplane. Some structure’s constraints are redundant, meaning that they are only active in regions where other constraints are also active. Geometrically, these hyperplanes only ‘touch’ the constraint cone, as is the case for the gray planes in Fig. 2a, which intersect the cone at extremal ray  $r_3$ . To assemble structures corresponding to redundant constraints,  $\hat{\xi}$  needs to be inside this intersection region. But in this region, the structures corresponding to the other active constraints will also

---

<sup>1</sup>This is not true if the  $\mathbf{M}$ -vectors of two structures are scalar multiples of each other, in which case their corresponding hyperplanes overlap completely and they can only be assembled together.

be present at finite density, making it impossible to exclusively assemble a structure corresponding to a redundant constraint. In our example, picking  $\hat{\xi}$  along  $r_3$  will result in high yield for the monomer, dimer, trimer, and tetramer and it is impossible to assemble the dimer or trimer on their own. Conversely, going along  $r_2$  results in a mixture of the tetramer and the red monomer and no additional structures, since these two structures correspond to the only active constraints at  $r_2$ .

### Polyhedral computation

We compute the face poset of the polyhedron in Fig. 3c with a simple version of the algorithm described in [40]. Briefly, we start by filtering the 283 constraints for redundancies using *cddlib* [41], which leaves us with 21 non-redundant constraints. We then use the double description algorithm [42, 43] to transform the cone from its inequality representation to its ray (vertex) representation. We can then construct an incidence matrix that indicates which rays are contained in which facets of the polyhedron. By generating the unique Boolean products of the columns of this matrix, we can iteratively construct all faces of the polyhedron.

### Predicting relative yield of the three rings

To find the direction in parameter space that allows tuning of the relative yields in Fig. 4, we construct the matrix  $M_{\text{rings}} = [\mathbf{M}_{\text{tri}}, \mathbf{M}_{\text{hex}}, \mathbf{M}_{\text{rho}}]^T$ . Computing the singular value decomposition of this matrix shows that it has rank two, equal to the codimension  $c_f$  of the corresponding face of the polyhedral constraint cone, as expected. Importantly, however, the vector  $\mathbb{1} = [1, 1, 1]^T$  lies in the image of  $M_{\text{rings}}$ , which means that there exists a direction in parameter space that raises the densities of the three rings uniformly and therefore does not affect relative yields. Projecting this direction out leaves us with a rank-one matrix whose right singular vector corresponding to the non-zero singular value is the direction in parameter space that controls the relative yields between the three rings.

We do not model the microscopic interaction between particles, and therefore cannot exactly

calculate the value of  $\Omega_s$  for the three rings. We therefore estimate the rings' entropic partition functions as

$$\Omega_s^{\text{rings}} \approx \frac{4\pi v_{\text{eff}}^{n_s-1}}{\lambda^D n_s \sigma_s}, \quad (8)$$

where  $v_{\text{eff}}$  is the effective volume a bound particle can explore if all other particles are held fixed and  $n_s$  is the number of particles in structure  $s$ . Importantly, this effective volume can be absorbed into the binding energies  $\epsilon$ , making them effective binding free energies  $\tilde{\epsilon} = \epsilon + kT \log(v_{\text{eff}}/\lambda^D)$ . This shows that  $v_{\text{eff}}$  can be compensated by changing  $\epsilon$ , which means that it cannot affect the range of possible relative yields and that we do not need to estimate  $v_{\text{eff}}$  for the predictions we make in the main text. Therefore, in this approximation, the shapes of the relative yield curves are determined by the structure compositions and the symmetry numbers  $\sigma_{\text{hex}} = 6$ ,  $\sigma_{\text{tri}} = 3$ ,  $\sigma_{\text{rho}} = 2$ .

## Folding DNA origami

To assemble our DNA origami monomers, we make a solution with 50 nM of p8064 scaffold (Tilibit), 200 nM of each staple strand (Integrated DNA Technologies [IDT]; Nanobase structure 247 [44] for sequences), and 1x folding buffer. We then anneal this solution using a temperature protocol described below. Our folding buffer, from here on referred to as FoBX, contains 5 mM Tris Base, 1 mM EDTA, 5 mM NaCl, and  $X$  mM  $\text{MgCl}_2$ . We use a Tetrad (Bio-Rad) thermocycler to anneal our samples.

To find the best folding conditions for each sample, we follow a standard screening procedure to search multiple  $\text{MgCl}_2$  concentrations and temperature ranges [12, 45], and select the protocol that optimizes the yield of monomers while limiting the number of aggregates that form. All particles used in this study were folded at 17.5 mM  $\text{MgCl}_2$  with the following annealing protocol: (i) hold the sample at 65 °C for 15 minutes, (ii) ramp the temperature from 58 °C to 50 °C with steps of 1 °C per hour, (iii) hold at 50 °C until the sample can be removed for further processing.

## Agarose gel electrophoresis

We use agarose gel electrophoresis to assess the folding protocols and purify our samples with gel extraction. We prepare all gels by bringing a solution of 1.5% (w/w) agarose in 0.5X TBE to a boil in a microwave. Once the solution is homogeneous, we cool it to 60 °C using a water bath. We then add  $\text{MgCl}_2$  and SYBR-safe (Invitrogen) to have concentrations of 5.5 mM  $\text{MgCl}_2$  and 0.5x SYBR-safe. We pour the solution into an Owl B2 gel cast and add gel combs (20  $\mu\text{L}$  wells for screening folding conditions or 200  $\mu\text{L}$  wells for gel extraction), which cools to room temperature. A buffer solution of 0.5x TBE and 5.5 mM  $\text{MgCl}_2$ , chilled at 4 °C for an hour, is poured into the gel box. Agarose gel electrophoresis is run at 110 V for 1.5–2 hours in a 4 °C cold room. We scan the gel with a Typhoon FLA 9500 laser scanner (GE Healthcare) at 100  $\mu\text{m}$  resolution.

## Sample purification

After folding, we purify our DNA origami particles to remove all excess staples and misfolded aggregates using gel purification. If the particles have self-complementary interactions, they are diluted 2:1 with 1xFoB2 and held at 47 °C for 30 minutes to unbind higher-order assemblies. The folded particles are run through an agarose gel (now at a 1xSYBR-safe concentration for visualization) using a custom gel comb, which can hold around 2 mL of solution per gel. We use a blue fluorescent light table to identify the gel band containing the monomers. The monomer band is then extracted using a razor blade. We place the gel slices into a Freeze 'N Squeeze spin column (Bio-Rad), freeze it in a -20 °C freezer for 5 minutes, and then spin the solution down for 5 minutes at 12 krcf. The concentration of the DNA origami particles in the supernatant is measured using a Nanodrop (Thermo Scientific). We assume that the solution consists only of monomers, where each monomer has 8064 base pairs.

Since the concentration of particles obtained after gel purification is typically not high enough for assembly, we concentrate the solution using ultrafiltration [45]. First, a 0.5-mL Amicon 100-kDa ultrafiltration spin column (Millipore) is equilibrated by centrifuging down 0.5 mL of 1xFoB5 buffer at 5 krcf for 7 minutes. Then, the

DNA-origami solution is added and centrifuged at 14 krcf for 15 minutes. We remove the flow-through and repeat the process until all of the DNA origami solution is filtered. Finally, we flip the filter upside down into a new Amicon tube and spin down the solution at 1 krcf for 2 minutes. The concentration of the final DNA-origami solution is then measured using a Nanodrop.

## Assembly experiments

Assembly experiments are conducted with DNA-origami particle concentrations ranging from 10 nM to 50 nM for the ring experiments (Fig. 4b), and 6 nM to 10.5 nM for the small cluster experiments (Fig. 1c). Assembly solutions have volumes up to 30  $\mu\text{L}$  with the desired DNA origami concentration in a 1xFoB buffer with  $\text{MgCl}_2$  concentrations of 20 mM to 30 mM for the ring experiments and 20 mM for the small cluster experiments. During small cluster experiments, the solution is kept at room temperature. For ring experiments, the solution is placed in a 200  $\mu\text{L}$  PCR tube and loaded into a thermocycler (Bio-Rad), which is placed through a temperature ramp between 40  $^\circ\text{C}$  and 25  $^\circ\text{C}$ . The thermocycler lid is held at 100  $^\circ\text{C}$  to prevent condensation of water on the cap of the PCR tube.

## Negative-stain TEM

We first prepare a solution of uranyl formate (Ufo). We boil doubly distilled water to deoxygenate it and then mix in Ufo powder to create a 2% (w/w) Ufo solution. We cover the solution with aluminum foil to avoid light exposure and vortex it vigorously for 20 minutes, after which we filter the solution with a 0.2  $\mu\text{m}$  filter. Lastly, we divide the solution into 0.2 mL aliquots, which are stored in a -80  $^\circ\text{C}$  freezer until further use.

Before each negative-stain TEM experiment, we take a 0.2 mL Ufo aliquot out from the freezer to thaw at room temperature. We add 4  $\mu\text{L}$  of 1 M NaOH and vortex the solution vigorously for 15 seconds. The solution is centrifuged at 4  $^\circ\text{C}$  and 16 krcf for 8 minutes. We extract 170  $\mu\text{L}$  of the supernatant for staining and discard the rest.

The EM samples are prepared using FCF400-Cu grids (Electron Microscopy Sciences). We glow discharge the grid prior to use at -20 mA for 30 seconds at 0.1 mbar, using a Quorum Emitech K100X

glow discharger. We place 4  $\mu\text{L}$  of the sample on the carbon side of the grid for 1 minute to allow adsorption of the sample to the grid. During this time, 5  $\mu\text{L}$  and 18  $\mu\text{L}$  droplets of Ufo solution are placed on a piece of parafilm. After the adsorption period, the remaining sample solution is blotted on 11  $\mu\text{m}$  Whatman filter paper. We then touch the carbon side of the grid to the 5  $\mu\text{L}$  drop and blot it away immediately to wash away any buffer solution from the grid. This step is followed by picking up the 18  $\mu\text{L}$  Ufo drop onto the carbon side of the grid and letting it rest for 30 seconds to deposit the stain. The Ufo solution is then blotted and any excess fluid is vacuumed away. Grids are allowed to dry for a minimum of 15 minutes before insertion into the TEM.

We image the grids using an FEI Morgagni TEM operated at 80 kV with a Nanosprint5 CMOS camera (AMT). The microscope is operated at 80 kV and images are acquired between x3,500 to x5,600 magnification.

**Supplementary information.** Supplementary information, containing supplementary notes and examples, together with the description of numerical and experimental details, is available at [URL].

**Acknowledgements.** We thank Berith Isaac and Amanda Tiano for their technical support with electron microscopy and Scott Waitukaitis for helpful comments on the manuscript. TEM images were prepared and imaged at the Brandeis Electron Microscopy facility. M.C.H and C.P.G acknowledge funding by the Gesellschaft für Forschungsförderung Niederösterreich under project FTI23-G-011. T.E.V, D.H., and W.B.R. acknowledge support from the Brandeis University Materials Research Science and Engineering Center (MRSEC) under grant number NSF DMR-2011846. W.B.R. acknowledges support from the Smith Family Foundation.

## Declarations

### Conflict of interest

The authors do not declare any conflict of interest.

### Code availability

Structure enumeration was performed with the *Roly.jl* [25, 46] package developed by M.C.H and

C.P.G, which is available at <https://github.com/mxhbl/Roly.jl>. Polyhedral computation and linear programming were performed using the freely available *Convex.jl* [47], *Polyhedra.jl* [48] packages and *cddlib* [41] library.

## Data availability

Design files and folding conditions of DNA origami used in this work can be found in the repository Nanobase [44] and are accessible at <https://nanobase.org/structure/247>.

## Author contribution

M.C.H. and C.P.G. conceived of and developed the theory. M.C.H. performed the numerical calculations. T.E.V., D.H., and W.B.R. designed the experiments. T.E.V. and D.H. conducted the experiments. All authors analyzed the data and wrote the paper.

## Materials availability

Not applicable

## References

- [1] Mirkin, C. A., Letsinger, R. L., Mucic, R. C. & Storhoff, J. J. A DNA-based method for rationally assembling nanoparticles into macroscopic materials. *Nature* **382**, 607–609 (1996).
- [2] Wang, Y. *et al.* Colloids with valence and specific directional bonding. *Nature* **491**, 51–55 (2012).
- [3] Wang, Y. *et al.* Crystallization of DNA-coated colloids. *Nature Communications* **6**, 7253 (2015).
- [4] Rogers, W. B., Shih, W. M. & Manoharan, V. N. Using DNA to program the self-assembly of colloidal nanoparticles and microparticles. *Nature Reviews Materials* **1**, 16008 (2016).
- [5] Jacobs, W. M. & Rogers, W. B. Assembly of complex colloidal systems using dna. *arXiv preprint* arXiv:2409.08988 (2024).
- [6] Park, S. H. *et al.* Finite-Size, Fully Addressable DNA Tile Lattices Formed by Hierarchical Assembly Procedures. *Angewandte Chemie* **118**, 6759–6759 (2006).
- [7] Wei, B., Dai, M. & Yin, P. Complex shapes self-assembled from single-stranded DNA tiles. *Nature* **485**, 623–626 (2012).
- [8] Ke, Y., Ong, L. L., Shih, W. M. & Yin, P. Three-Dimensional Structures Self-Assembled from DNA Bricks. *Science* **338**, 1177–1183 (2012).
- [9] Evans, C. G., O’Brien, J., Winfree, E. & Murugan, A. Pattern recognition in the nucleation kinetics of non-equilibrium self-assembly. *Nature* **625**, 500–507 (2024).
- [10] Bai, X.-c., Martin, T. G., Scheres, S. H. W. & Dietz, H. Cryo-EM structure of a 3D DNA-origami object. *Proceedings of the National Academy of Sciences* **109**, 20012–20017 (2012).
- [11] Funke, J. J. & Dietz, H. Placing molecules with Bohr radius resolution using DNA origami. *Nature Nanotechnology* **11**, 47–52 (2016).
- [12] Hayakawa, D. *et al.* Geometrically programmed self-limited assembly of tubules using DNA origami colloids. *Proceedings of the National Academy of Sciences* **119**, e2207902119 (2022).
- [13] Hayakawa, D., Videbæk, T. E., Grason, G. M. & Rogers, W. B. Symmetry-Guided Inverse Design of Self-Assembling Multiscale DNA Origami Tilings. *ACS Nano* **18**, 19169–19178 (2024).
- [14] Sigl, C. *et al.* Programmable icosahedral shell system for virus trapping. *Nature Materials* **20**, 1281–1289 (2021).
- [15] Wei, W.-S. *et al.* Hierarchical assembly is more robust than egalitarian assembly in synthetic capsids. *Proceedings of the National Academy of Sciences* **121**, e2312775121 (2024).

- [16] Videbæk, T. E. *et al.* Measuring multisubunit mechanics of geometrically-programmed colloidal assemblies via cryo-EM multi-body refinement. *arXiv* (2025).
- [17] Sacanna, S., Irvine, W. T. M., Chaikin, P. M. & Pine, D. J. Lock and key colloids. *Nature* **464**, 575–578 (2010).
- [18] Huntley, M. H., Murugan, A. & Brenner, M. P. Information capacity of specific interactions. *Proceedings of the National Academy of Sciences* **113**, 5841–5846 (2016).
- [19] Huang, P.-S., Boyken, S. E. & Baker, D. The coming of age of de novo protein design. *Nature* **537**, 320–327 (2016).
- [20] Boyken, S. E. *et al.* De novo design of protein homo-oligomers with modular hydrogen-bond network-mediated specificity. *Science* **352**, 680–687 (2016).
- [21] Niu, R. *et al.* Magnetic handshake materials as a scale-invariant platform for programmed self-assembly. *Proceedings of the National Academy of Sciences* **116**, 24402–24407 (2019).
- [22] Bohlin, J., Turberfield, A. J., Louis, A. A. & Sulc, P. Designing the Self-Assembly of Arbitrary Shapes Using Minimal Complexity Building Blocks. *ACS Nano* **17**, 5387–5398 (2023).
- [23] Videbæk, T. E. *et al.* Economical routes to size-specific assembly of self-closing structures. *Science Advances* **10**, eado5979 (2024).
- [24] Duque, C. M. *et al.* Limits of economy and fidelity for programmable assembly of size-controlled triply periodic polyhedra. *Proceedings of the National Academy of Sciences* **121**, e2315648121 (2024).
- [25] Hübl, M. C. & Goodrich, C. P. Accessing Semi-Addressable Self Assembly with Efficient Structure Enumeration. *arXiv* (2024).
- [26] Murugan, A., Zou, J. & Brenner, M. P. Undesired usage and the robust self-assembly of heterogeneous structures. *Nature Communications* **6**, 6203 (2015).
- [27] Sartori, P. & Leibler, S. Lessons from equilibrium statistical physics regarding the assembly of protein complexes. *Proceedings of the National Academy of Sciences* **117**, 114–120 (2020).
- [28] Osat, S. & Golestanian, R. Non-reciprocal multifarious self-organization. *Nature Nanotechnology* **18**, 79–85 (2023).
- [29] Arkus, N., Manoharan, V. N. & Brenner, M. P. Deriving Finite Sphere Packings. *SIAM Journal on Discrete Mathematics* **25**, 1860–1901 (2011).
- [30] Klein, E. D., Perry, R. W. & Manoharan, V. N. Physical interpretation of the partition function for colloidal clusters. *Physical Review E* **98**, 032608 (2018).
- [31] Curatolo, A. I., Kimchi, O., Goodrich, C. P., Krueger, R. K. & Brenner, M. P. A computational toolbox for the assembly yield of complex and heterogeneous structures. *Nature Communications* **14**, 8328 (2023).
- [32] Holmes-Cerfon, M., Gortler, S. J. & Brenner, M. P. A geometrical approach to computing free-energy landscapes from short-ranged potentials. *Proceedings of the National Academy of Sciences* **110**, E5–E14 (2013).
- [33] Hagan, M. F. & Grason, G. M. Equilibrium mechanisms of self-limiting assembly. *Reviews of Modern Physics* **93**, 025008 (2021).
- [34] Kardar, M. *Statistical Physics of Particles* (Cambridge University Press, 2007).
- [35] Ziegler, G. M. *Lectures on Polytopes* Graduate Texts in Mathematics (Springer New York, 1995).
- [36] Grünbaum, B. *Convex Polytopes* Graduate Texts in Mathematics (Springer New York, 2003).

- [37] Barvinok, A. *A Course in Convexity* Graduate Studies in Mathematics (American Mathematical Society, 2002).
- [38] Fukuda, K. *Polyhedral Computation* (Department of Mathematics, Institute of Theoretical Computer Science ETH Zurich, 2020). URL [doi.org/10.3929/ethz-b-000426218](https://doi.org/10.3929/ethz-b-000426218).
- [39] Boyd, S. & Vandenberghe, L. *Convex optimization* (Cambridge university press, 2004).
- [40] Fukuda, K. & Rosta, V. Combinatorial face enumeration in convex polytopes. *Computational Geometry* **4**, 191–198 (1994).
- [41] Fukuda, K. *et al.* Cddlib. <https://github.com/cddlib/cddlib> (2020).
- [42] Motzkin, T. S., Raiffa, H., Thompson, G. L. & Thrall, R. M. in *The double description method* (eds Kuhn, H. W. & Tucker, A. W.) *Contributions to the Theory of Games, Volume II* 51–74 (Princeton University Press, Princeton, 1953). URL <https://doi.org/10.1515/9781400881970-004>.
- [43] Fukuda, K. & Prodon, A. Deza, M., Euler, R. & Manoussakis, I. (eds) *Double description method revisited*. (eds Deza, M., Euler, R. & Manoussakis, I.) *Combinatorics and Computer Science*, 91–111 (Springer Berlin Heidelberg, Berlin, Heidelberg, 1996).
- [44] Poppleton, E., Mallya, A., Dey, S., Joseph, J. & Šulc, P. Nanobase.org: a repository for DNA and RNA nanostructures. *Nucleic acids research* **50**, D246–D252 (2022).
- [45] Wagenbauer, K. F. *et al.* How we make DNA origami. *ChemBioChem* **18**, 1873–1885 (2017).
- [46] Hübl, M. C. & Goodrich, C. P. Roly.jl: Reverse-search polyform enumerator. <https://github.com/mxhbl/Roly.jl> (2024).
- [47] Udell, M. *et al.* Convex optimization in Julia. *SC14 Workshop on High Performance Technical Computing in Dynamic Languages* (2014).
- [48] Legat, B. Polyhedra.jl. <https://github.com/JuliaPolyhedra/Polyhedra.jl> (2023).

# Supplementary Information: The hidden architecture of equilibrium self-assembly

Maximilian C. Hübl<sup>1</sup>, Thomas E. Videbæk<sup>2</sup>, Daichi Hayakawa<sup>2</sup>,  
W. Benjamin Rogers<sup>2\*</sup>, Carl P. Goodrich<sup>1\*</sup>

<sup>1</sup>Institute of Science and Technology Austria (ISTA), Am Campus 1,  
Klosterneuburg, 3400, Austria.

<sup>2</sup>Martin A. Fisher School of Physics, Brandeis University, Waltham,  
02453, Massachusetts, USA.

\*Corresponding author(s). E-mail(s): [wrogers@brandeis.edu](mailto:wrogers@brandeis.edu);  
[carl.goodrich@ist.ac.at](mailto:carl.goodrich@ist.ac.at);  
Contributing authors: [maximilian.huebl@ist.ac.at](mailto:maximilian.huebl@ist.ac.at);  
[videbaek@brandeis.edu](mailto:videbaek@brandeis.edu); [dhayakawa@brandeis.edu](mailto:dhayakawa@brandeis.edu);

## Supplementary Methods

### Numerical yield optimization

Figure 2b of the main text shows the yields of designable structures along a particular direction in parameter space, together with the maximally achievable yields of non-designable structures as a function of binding energy  $\varepsilon$ . We compute these maximally achievable yields through a non-linear optimization that we now explain.

The yield of a structure  $s$  can be written as

$$Y_s(\boldsymbol{\xi}) = \frac{\Omega_s e^{M_s \cdot \boldsymbol{\xi}}}{\sum_{s'} \Omega_{s'} e^{M_{s'} \cdot \boldsymbol{\xi}}} = [1 + R_s(\boldsymbol{\xi})]^{-1}, \quad (1)$$

with

$$R_s(\boldsymbol{\xi}) = \sum_{s' \neq s} \frac{\Omega_{s'}}{\Omega_s} e^{(M_{s'} - M_s) \cdot \boldsymbol{\xi}}. \quad (2)$$

Maximizing  $Y_s(\boldsymbol{\xi})$  is clearly equivalent to minimizing  $R_s(\boldsymbol{\xi})$ , and since  $R_s(\boldsymbol{\xi})$  is a convex function, we can formulate yield optimization as a convex optimization problem [1]. Using convex optimizers, we can also impose physical constraints on the optimization

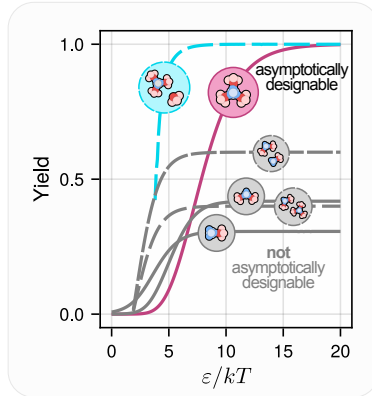


**Fig. S1** Yield of various structures from the assembly system of Fig 2a of the main text. Yields of individual structures (solid) and pairs of structures (dashed) are shown as a function of binding energy  $\varepsilon$ . All yields were optimized through the convex optimization discussed in the text. The results are very similar to Fig 2b, the main difference being that yields of the asymptotically designable structures rise at lower energies. The gray yield curves are identical to those shown in Fig 2b of the main text.

process. For the gray yield curves in Fig. 2b of the main text, we constrain the maximal allowable binding energy to the respective values on the  $x$ -axis and constrain the maximum allowable particle volume fraction to 20%. For pairs of structures, we also constrain their relative yields to be 1 : 1. Interestingly, these constraints cannot always be satisfied simultaneously, which is why the yield curves of the structure pairs terminate at  $\varepsilon \approx 2 kT$ .

In Fig. 2b of the main text, the yields of the designable structures have been calculated by following a linear direction in parameter space, which means that the total particle volume fraction along the colored curves is not constant, but decreases as the binding energy increases. For completeness, we show in Fig. S1 the yields of all structures optimized through convex optimization, where the volume fraction is fixed to 20% at all energies. Comparing Fig. S1 to Fig. 2b of the main text shows that for the designable structures, non-linear optimization achieves high yields at lower binding energies. This shows that the speed at which the asymptotic limit is reached can be further optimized.

## Intersections of designable sets

As mentioned in the main text, the correspondence between designable sets of structures and polyhedral faces implies that the intersection of two designable sets is also designable. To see this, consider two designable sets  $\mathcal{S}_f$  and  $\mathcal{S}_g$ , their corresponding faces  $f$  and  $g$ , and their conic combination  $f + g = \{\alpha x + \beta y \mid x \in f, y \in g, \alpha, \beta \geq 0\} \equiv \{x + y \mid x \in f, y \in g\}$ . We will show that the designable set corresponding to  $f + g$  is given by the intersection of  $\mathcal{S}_f$  and  $\mathcal{S}_g$ .

First note that the designable set  $\mathcal{S}_f$  consists of the structures  $s \in \mathcal{S}$  for which  $\mathbf{M}_s \cdot x = 0$  for all  $x \in f$ , or, more formally,

$$\mathcal{S}_f = \{s \in \mathcal{S} \mid \mathbf{M}_s \cdot x = 0 \text{ for all } x \in f\}. \quad (3)$$

Similarly,  $\mathcal{S}_{f+g}$  is given by

$$\mathcal{S}_{f+g} = \{s \in \mathcal{S} \mid \mathbf{M}_s \cdot (x + y) = 0 \text{ for all } x \in f, y \in g\}. \quad (4)$$

Since  $f$  and  $g$  are faces of the cone,  $\mathbf{M}_s \cdot x \leq 0$  and  $\mathbf{M}_s \cdot y \leq 0$ , which implies that  $\mathbf{M}_s \cdot (x + y) = 0$  if and only if  $\mathbf{M}_s \cdot x = 0$  and  $\mathbf{M}_s \cdot y = 0$ . This means that a structure  $s$  is in  $\mathcal{S}_{f+g}$  if and only if  $s \in \mathcal{S}_f$  and  $s \in \mathcal{S}_g$ , and therefore

$$\mathcal{S}_{f+g} = \mathcal{S}_f \cap \mathcal{S}_g. \quad (5)$$

Note that  $f + g$  is not necessarily a face of the cone, but may only be a subset of a face. If this is the case, then there exists at least one other face  $h$ , such that  $\mathcal{S}_f \cap \mathcal{S}_g \cap \mathcal{S}_h = \mathcal{S}_f \cap \mathcal{S}_g$  and the complete face corresponding to  $\mathcal{S}_f \cap \mathcal{S}_g$  is given by  $f + g + h$ .

The fact that the intersection of designable sets is again designable also has important implications for non-designable sets. While thermodynamic constraints prevent high yield for any non-designable set of structures, the intersection property of designable sets guarantees that any non-designable set is contained in a unique *minimal designable set*. This is readily proved by noting that if there were two different minimal designable sets that contain the non-designable target(s), we could form their intersection to obtain a smaller containing set.

## Note on negative binding energies

Fig. 2a of the main text shows that the allowed limit directions include directions where the binding energies approach  $-\infty$ . A negative binding energy for a certain bond means that this ‘bond’ is actually repulsive and that structures that contain this bond are less likely to form. In the limit  $\varepsilon \rightarrow -\infty$ , this means that a structure containing a ‘repulsive bond’ cannot form and can be safely neglected.

The same approximation is already made implicitly in the enumeration step: we assume that only particles with complementary binding sites are able to bind – assuming that the yield of all structures with undesired bonds is exactly zero corresponds to setting the binding energy of all those undesired bonds to  $-\infty$ . Taking a “negative energy” limit is therefore equivalent to removing a bond from the binding rules. If one wishes to enumerate only those designable structures that contain all bond types, one can simply add additional inequality constraints that force energies to be non-negative, i.e., a constraint of the form  $\varepsilon \geq 0$ .

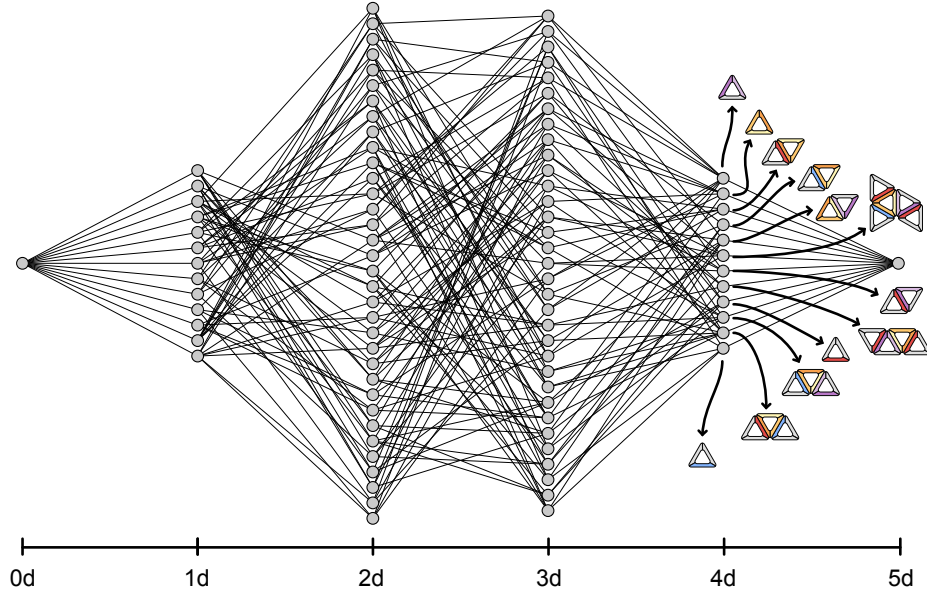


**Fig. S2** Hasse diagram of the system shown in Fig. 1c of the main text, with the additional constraint that all four binding energies are equal. The twelve individually designable structures are shown next to their corresponding nodes in the diagram.

### Note on independent absolute and relative yields

As mentioned in the main text, the relative yields within a designable set can be tuned independently of the absolute yield of the set. However, changing relative yields by tuning  $\xi_{\perp}$  *does* affect the absolute yield of the set. This is true for designable and non-designable sets of structures alike. What makes designable sets special is that there exists a direction  $\hat{\xi}$  in parameter space along which the absolute yield of the set increases, but the relative yields between the structures in the set remain the same. This means that while changing  $\xi_{\perp}$  does affect the absolute yield of a designable set, it is always possible to compensate for this by tuning  $\lambda$ .

### Additional example systems

In this supplemental section, we briefly describe the architectures and some designable structures of additional example systems.

#### *Small clusters*

For completeness, we briefly discuss the designable structures resulting from the binding rules of the system in Fig. 1c of the main text. This system only leads to 16 possible structures, but still has eight degrees of freedom to tune yields. This large amount of control leads to all 16 structures being asymptotically designable. Note that we distinguish between a “shape” and a “structure”: any two dimers, for example, are the same

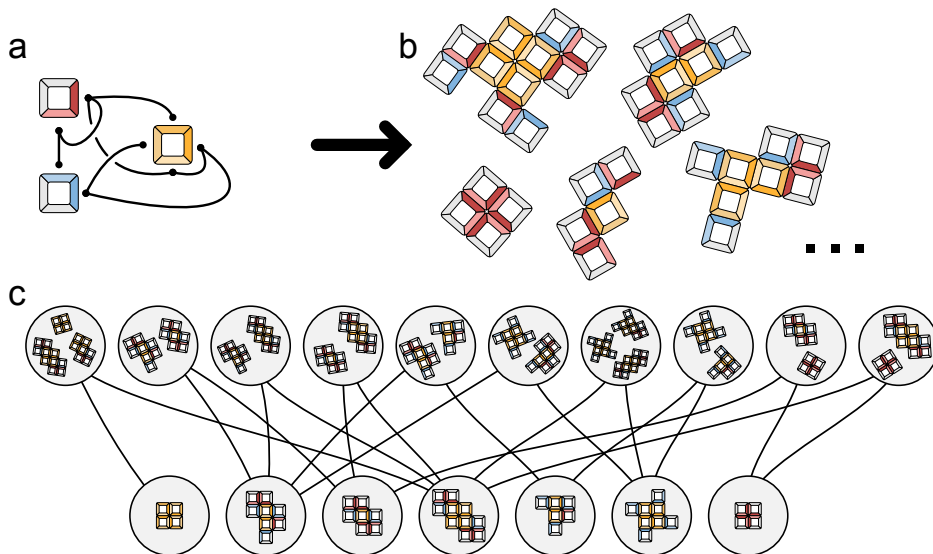


**Fig. S3** Analysis of a non-deterministic system with square building blocks. (a) Binding rules between three square building blocks. (b) Some of the 677 possible structures. (c) Section of the Hasse diagram, showing all non-monomer individually designable structures (bottom row) and the pairs and triplets containing them (upper row).

shape, but if the particle types differ at all, then they are different structures. Experimentally, it is much easier to differentiate between shapes than between structures, which is why in Fig. 2c of the main text we show the yield of the 7 distinct shapes.

However, the situation becomes more interesting when we introduce further constraints on the parameters, for example, by imposing that the four distinct programmable bonds have equal binding energies, which is a practical constraint often encountered in experimental systems. We can easily incorporate this constraint simply by stopping to distinguish the different types of bonds that the structures contain.

In this case, there are twelve designable structures and 33 designable sets in the next level of the architecture, most of which correspond to pairs of structures. The Hasse diagram, together with the individually designable structures, is shown in Fig. S2.

### *Non-deterministic structures from square building blocks*

In this section we briefly outline how asymptotic designability can help with economical and multifarious assembly. For this, we use square-shaped building blocks with a set of binding rules that is similar to one that we previously investigated numerically in Ref. [2]. These highly non-deterministic and promiscuous binding rules are shown in Fig. S3a and lead to 677 possible structures, some of which are shown in Fig. S3b. We add the extra constraint that all binding energies have to be equal, leading to a

four-dimensional parameter space. Since the binding rules are rather complicated and many resulting structures share the same building blocks and bonds, it is difficult to predict which of the 677 structures can be assembled at high yield.

However, by exploiting the architecture of the constraint cone, we can immediately enumerate not only the individually designable structures, but also all designable sets, regardless of their size. The whole calculation, including the initial enumeration of the 677 possible structures, takes less than a second on a typical laptop computer. A subsection of the Hasse diagram is shown in Fig. S3c, which shows all non-monomer individually designable structures, and some of the designable pairs and triplets.

The list of designable structures shows that the chosen binding rules can lead to multifarious assembly of different targets. Moreover, since all binding energies are set to be equal, it is, in principle, possible to assemble either of these structures by tuning the concentration of the building blocks.

## Supplemental experimental data

Here we provide supplemental experimental data for the experimental results shown in Fig. 1c and Fig. 4b of the main text. Figure S4 contains details about the design of the building blocks and the programmable bonds. Table 1 contains the experimental conditions and structure counts for the small cluster experiments shown in Fig. 1c. Table 2 contains the experimental conditions and structure counts for the ring experiments shown in Fig. 4b. Figure S5 and Fig. S6 contain representative TEM images from the small cluster and ring experiments respectively. Table 3, Table 4, and Table 5 show the interaction sequences for the different experiments.

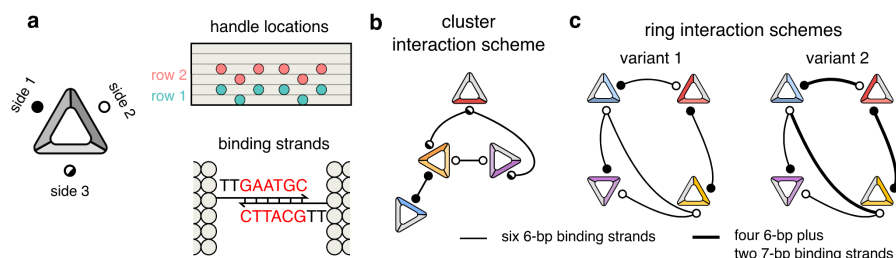


**Fig. S4 Design of self-assembly experiments.** (a) Sketch of where interactions are located on the triangular monomer. Each side of the triangle has a set of 12 staples that can be extruded from the face of the DNA-origami particle. (b) Binding scheme used for the cluster experiments shown in Fig. 1c of the main text. Sequences for these interactions are shown in Table 3 (c) Binding schemes for the ring experiments shown in Fig. 4 of the main text. For these experiments we have two variants, the second of which we intentionally make the interactions with the purple particle weaker relative to the other interactions. Sequences for these interactions are shown in Table 4 and 5.

**Table 1: Experimental conditions for cluster assemblies.**

$c_0$  is the concentration for the blue, yellow, and purple particles.  $c_{\text{red}}$  is the concentration for the red particle.  $N_{\text{mono}}$  is the counts of monomers, Fig. S5d.  $N_{\text{dimer}}$  is the counts of dimers, Fig. S5d.  $N_{\text{trimer}}$  is the counts of trimers, Fig. S5e.  $N_{\text{triangle}}$  is the counts of triangular tetramers, Fig. S5c.  $N_{\text{concave}}$  is the counts of concave tetramers, Fig. S5b.  $N_{\text{mono}}$  is the counts of linear tetramers, Fig. 1c.  $N_{\text{boat}}$  is the counts of fully formed pentamers, Fig. S5a.

$c_0$ [nM]	$c_{\text{red}}$ [nM]	MgCl <sub>2</sub> [mM]	$N_{\text{mono}}$	$N_{\text{dimer}}$	$N_{\text{trimer}}$	$N_{\text{triangle}}$	$N_{\text{concave}}$	$N_{\text{line}}$	$N_{\text{boat}}$
2	0	20	159	131	339	2	5	0	0
2	1	20	157	94	246	72	75	7	13
2	2	20	172	97	171	125	114	17	72
2	3	20	201	104	164	69	74	28	122
2	4	20	75	30	49	30	20	15	90
2	5	20	189	49	39	25	18	17	141

**Table 2: Experimental conditions for ring assemblies.**

$c_{\text{R,B,Y}}$  is the concentration for the red, blue, and yellow particles.  $c_{\text{P}}$  is the concentration for the purple particle. Under “Interaction type” we use “Equal” to denote the six-base interactions in Table 4 and “Biased” to denote the seven-base biased interactions in Table 5.  $N_t$ ,  $N_r$ ,  $N_h$  are the counts for the triangular, rhombic, and hexagonal rings that we observed.

Exp. No.	$c_{\text{R,B,Y}}$ [nM]	$c_{\text{P}}$ [nM]	MgCl <sub>2</sub> [mM]	Interaction type	$N_t$	$N_r$	$N_h$
1	10	0	30	Equal	0	0	35
2	10	2	30	Equal	7	42	58
3	10	4	30	Equal	36	24	5
4	10	6	30	Equal	56	35	3
5	10	8	30	Equal	95	59	3
6	10	10	30	Equal	65	32	2
7	10	1	20	Equal	2	14	80
8	10	2	20	Equal	35	67	67
9	10	3	30	Equal	34	47	16
10	10	5	25	Biased	1	6	48
11	10	10	25	Biased	2	22	41
12	10	15	25	Biased	7	17	35
13	10	20	25	Biased	5	13	28
14	10	10	25	Biased	31	65	83
15	10	20	25	Biased	34	42	33
16	5	20	25	Biased	24	50	22
17	5	30	25	Biased	7	22	8
18	10	10	30	Biased	21	46	49

Exp. No.	$c_{R,B,Y}$ [nM]	$c_P$ [nM]	$MgCl_2$ [mM]	Interaction type	$N_t$	$N_r$	$N_h$
19	10	20	30	Biased	30	66	40

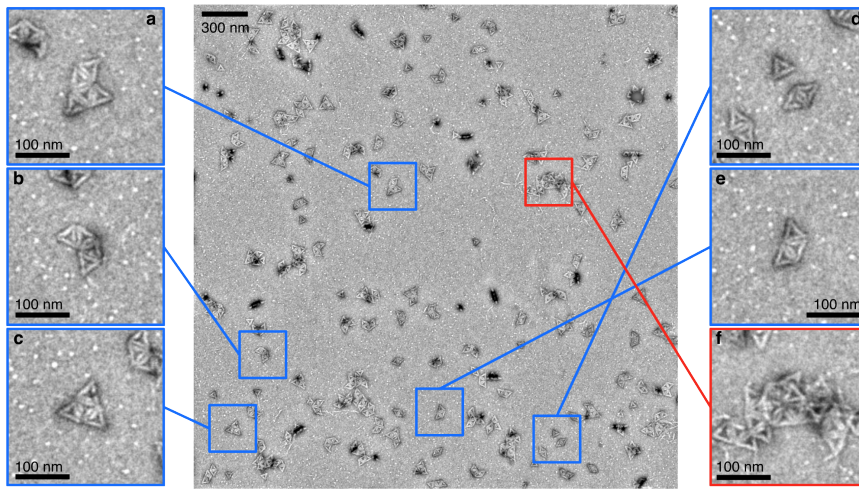


**Fig. S5 Representative TEM image from a cluster experiment.** The center image is a 1500x1500 pixel subregion from a 2560x2048 pixel experimental TEM image. Panels (a)-(e) show different clusters that can be seen in the image, the only one that is missing here is the linear tetramer shown in Fig. 1c. Occasionally we find overlapping clusters, shown in (f). These most likely do to sample preparation and are not included in our statistics. The TEM image has been bandpass filtered to enhance contrast.

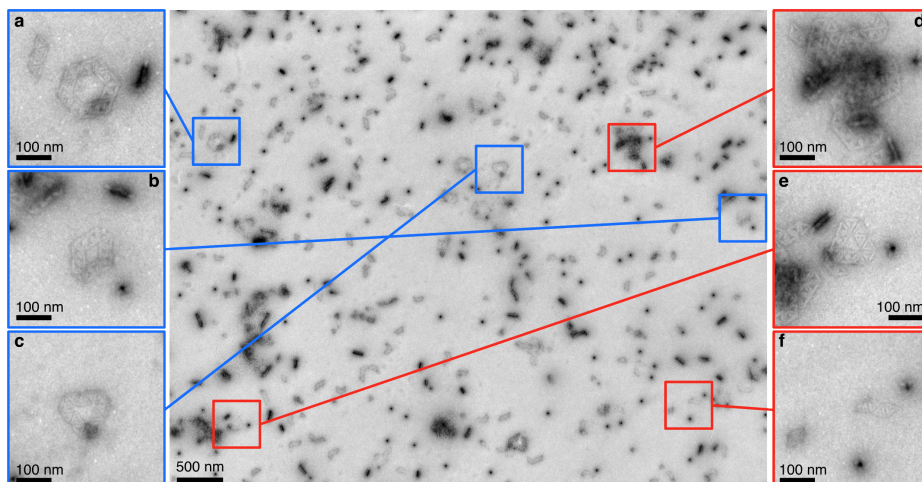


**Fig. S6 Representative TEM image from a ring experiment.** The center image is the size of the field of view that we take experimental TEM images. In this image, we can see several different features of our assembly experiments. Panels (a)-(c) show the three varieties of ring structures that we targeted. However, the majority of the field of view is filled with incomplete assemblies or artifacts from sample preparation. For instance, panel (d) shows an agglomeration that we typically ascribe to the clumping of structures induced by staining the sample with UFO and then drying it. We also observe structures that overshoot an intended target, as in panel (e), due to the flexibility of the DNA-origami intersubunit bonds; assemblies of triangles are not necessarily constrained to be planar. Finally, the predominant things we find are monomers or small oligomers, shown in panel (f).

**Table 3: Side interactions for small cluster assembly.** A list of the set of six interaction sequences that make up a side interaction of a monomer. The sequences are for self-complementary side interactions, e.g. Position 1 binds to Position 6, Position 2 binds to Position 5, and Position 3 binds to Position 4.

Particle	Side	Row	Position 1	Position 2	Position 3	Position 4	Position 5	Position 6
Blue	1	2	CAATAG	TGATTG	CTAGGA	CACATC	ACGAAG	ACCTGA
Yellow	1	2	TCAGGT	CTTCGT	GATGTG	TCCTAG	CAATCA	CTATTG
	2	2	ATGACA	TACAGG	AACCTA	GAGACA	GACAGA	ACTAAC
Purple	3	2	GTACAT	AGTCAG	CGATGG	CTTACT	AGTATC	GTATGT
	2	2	GTTAGT	TCTGTC	TGTCTC	TAGGTT	CCTGTA	TGTCAT
Red	3	2	GTACAT	AGTCAG	CGATGG	CTTACT	AGTATC	GTATGT
	3	2	ACATAC	GATACT	AGTAAG	CCATCG	CTGACT	ATGTAC

**Table 4: Side interactions for ring assembly: Variant 1.** A list of the set of six interaction sequences that make up a side interaction of a monomer. The sequences are for self-complimentary side interactions, e.g. Position 1 binds to Position 6, Position 2 binds to Position 5, and Position 3 binds to Position 4.

Particle	Side	Row	Position 1	Position 2	Position 3	Position 4	Position 5	Position 6
Red	1	2	CAATAG	TGATTG	CTAGGA	CACATC	ACGAAG	ACCTGA
	2	2	AGATAG	TTCCTG	TTCCAT	GATATG	ATGCAC	AACATT
Blue	1	2	GTTAGT	TCTGTC	TGTCTC	TAGGTT	CCTGTA	TGTCAT
	1	1	GTACGA	TCACAG	TGAGAA	GAATCT	GGAATA	AGATGC
Yellow	2	2	AATGTT	GTGCAT	CATATC	ATGGAA	CAGGAA	CTATCT
	1	2	ATCTAC	CTCAAG	CTGAAT	CAGAAT	TAATCG	GGAACT
Purple	1	1	GCATCT	TATTCC	AGATTC	TTCTCA	CTGTGA	TCGTAC
	2	2	AATGTT	GTGCAT	CATATC	ATGGAA	CAGGAA	CTATCT
Purple	1	2	AGTTCC	CGATTA	ATTCTG	ATTCAG	CTTGAG	GTAGAT
	2	2	ATGACA	TACAGG	AACCTA	GAGACA	GACAGA	ACTAAC

**Table 5: Side interactions for ring assembly: Variant 2.** A list of the set of six interaction sequences that make up a side interaction of a monomer. The sequences are for self-complimentary side interactions, e.g. Position 1 binds to Position 6, Position 2 binds to Position 5, and Position 3 binds to Position 4.

Particle	Side	Row	Position 1	Position 2	Position 3	Position 4	Position 5	Position 6
Red	1	2	CAATAG	TGATTG	CTAGGAG	CACATCG	ACGAAG	ACCTGA
	2	2	GGATAA	TCATCC	AGATTCG	TTCTCAG	ACTGAG	AGAGAT
Blue	1	2	AGTTCC	CGATTA	ATTCTGG	ATTCAGG	CTTGAG	GTAGAT
	1	1	ATGACA	TACAGG	AACCTA	GAGACA	GACAGA	ACTAAC
Yellow	2	2	TCAGGT	CTTCGT	CGATGTG	CTCCTAG	CAATCA	CTATTG
	1	2	ATCTAC	CTCAAG	CCTGAAT	CCAGAAT	TAATCG	GGAACT
Purple	1	1	AGATAG	TTCCTG	TTCCAT	GATATG	ATGCAC	AACATT
	2	2	ATCTCT	CTCAGT	CTGAGAA	CGAATCT	GGATGA	TTATCC
Purple	1	1	AATGTT	GTGCAT	CATATC	ATGGAA	CAGGAA	CTATCT
	2	1	GTTAGT	TCTGTC	TGTCTC	TAGGTT	CCTGTA	TGTCAT

## References

- [1] Boyd, S. & Vandenberghe, L. *Convex optimization* (Cambridge university press, 2004).
- [2] Hübl, M. C. & Goodrich, C. P. Accessing Semi-Addressable Self Assembly with Efficient Structure Enumeration. *arXiv* (2024).